Supplemental Information

Supplemental Table 1. TMEsig-score of nonsquamous NSCLC cell lines in CCLE dataset.

Supplemental Table 2. Summary of Clinical characteristics of patients with nonsquamous NSCLC cancer in 9 datasets.

Supplemental Table 3. Clinical annotation and TME infiltration pattern of the individual patient in meta-GEO cohort.

Supplemental Table 4. Clinical annotation and TME infiltration pattern of the individual patient in TCGA-LUAD cohort.

Supplemental Table 5. Prognostic analysis of 657 TME phenotype-related DEGs using a univariate Cox analysis.

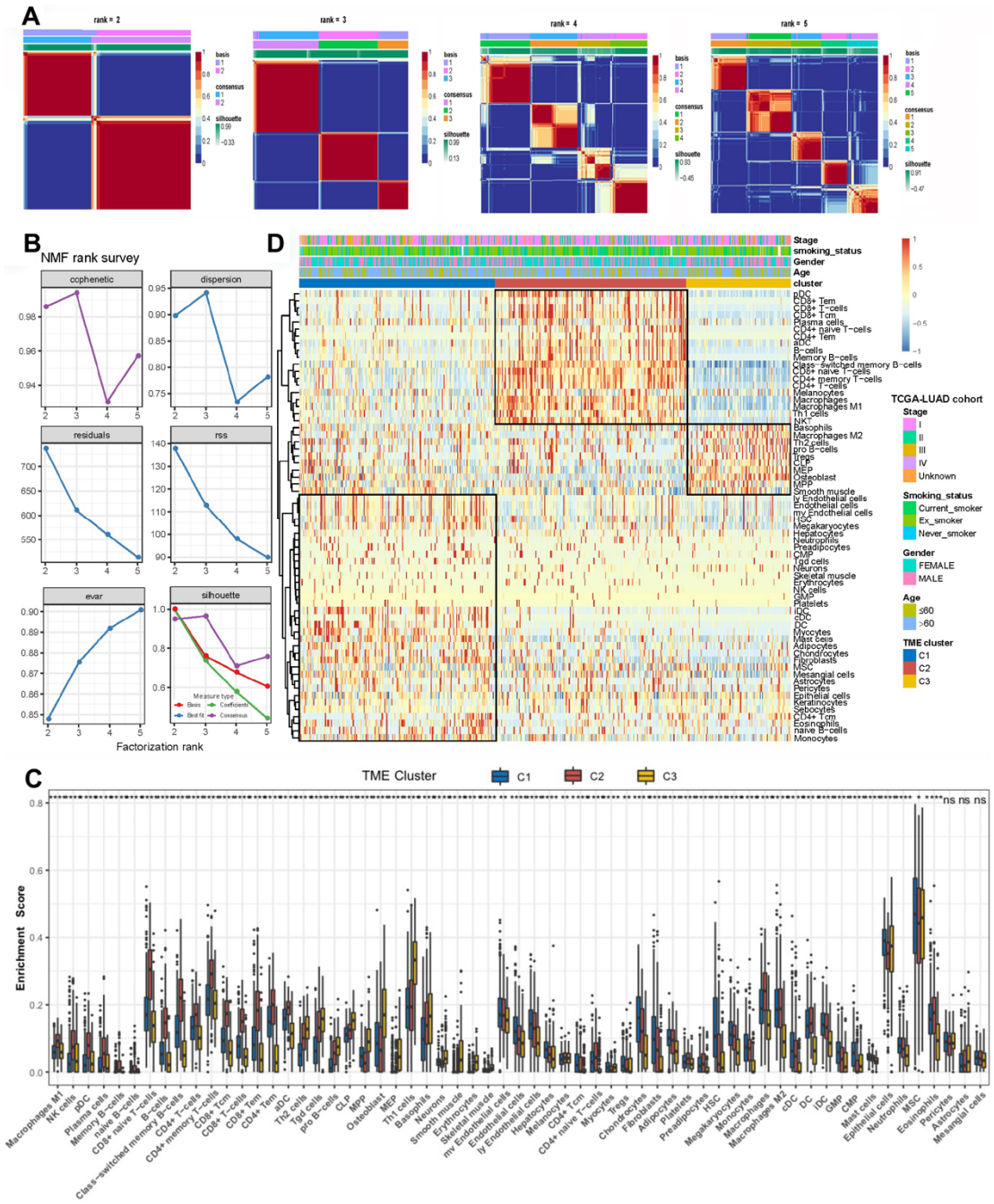

Supplemental Figure 1. Consensus clustering of TME cell infiltration patterns in the lung cancer. (A) Heatmap representation of NMF clustering for TME infiltration pattern in meta-GEO with cluster numbers from 2 to 5. **(B)** The relationship between cophenetic, dispersion, residuals, evar, and silhouette coefficients with respect to number of clusters. **(C)** Comparison of the enrichment score of xCell-annotated cell subpopulations among three TME clusters in meta-GEO cohort. The Kruskal-Wallis

test was used to test the statistical differences among three gene clusters and the asterisks represented the statistical P-value (ns; not significant; *P < 0.05; **P < 0.01; ***P < 0.001). **(D)** Identification of TME cell-infiltration pattern in the TCGA-LUAD cohort. Clinicopathological information including age, gender, smoking status and tumor stage, as well as TME cluster, is shown in annotations above.

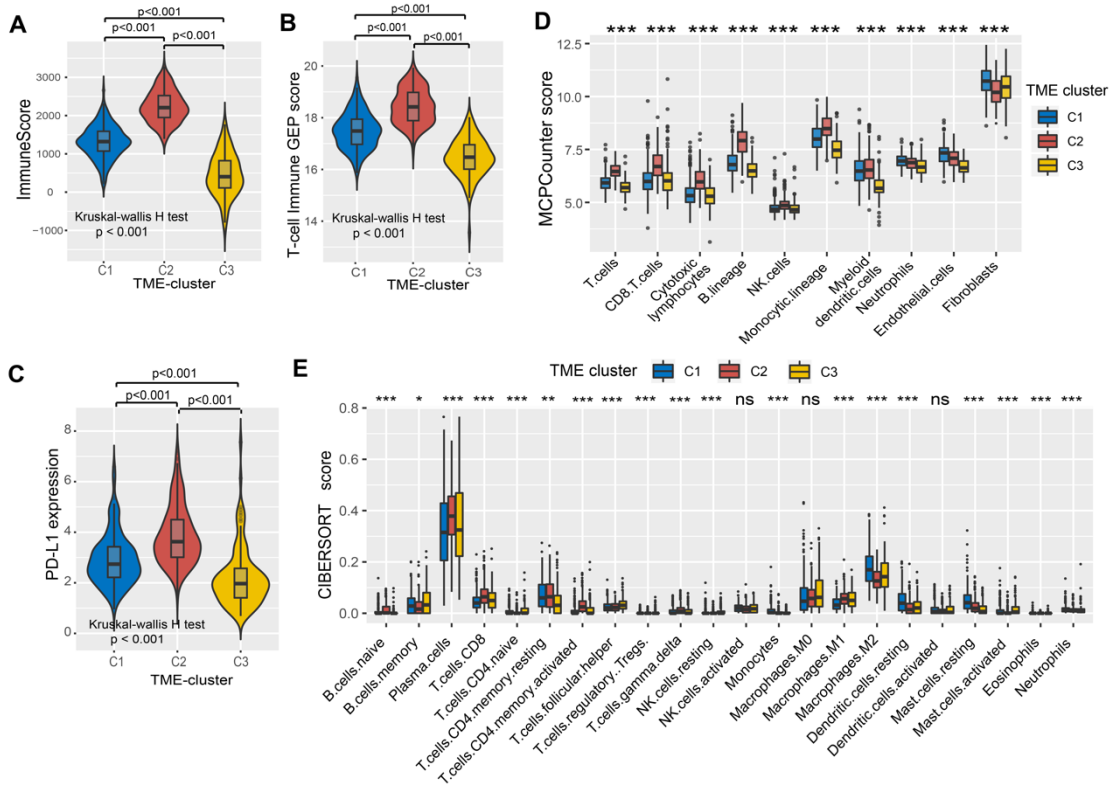

Supplemental Figure 2. Comparison of immune signatures in the identified TME clusters. Differences in Immune score **(A)**, T cell-inflamed GEP score **(B)**, and PD-L1 expression **(C)** among three TME clusters in TCGA-LUAD cohort. The Kruskal-Wallis test was used to compare the statistical difference between three TME clusters ($P < 0.001$). **(D)** Comparison of immune cell and stromal cell subsets calculated by MPC-Counter algorithm between the three TME cell-infiltration patterns. **(E)** Comparison of immune cell level inferred by CIBERSORT algorithm between the three TME cell-infiltration patterns. Within each group, the thick line represents the median value. The bottom and top of the boxes are the 25th and 75th percentiles (interquartile range). The whiskers encompass 1.5 times the interquartile range. The range of P values are labeled above each boxplot with asterisks (*$P < 0.05$, **$P < 0.01$, ***$P < 0.001$).

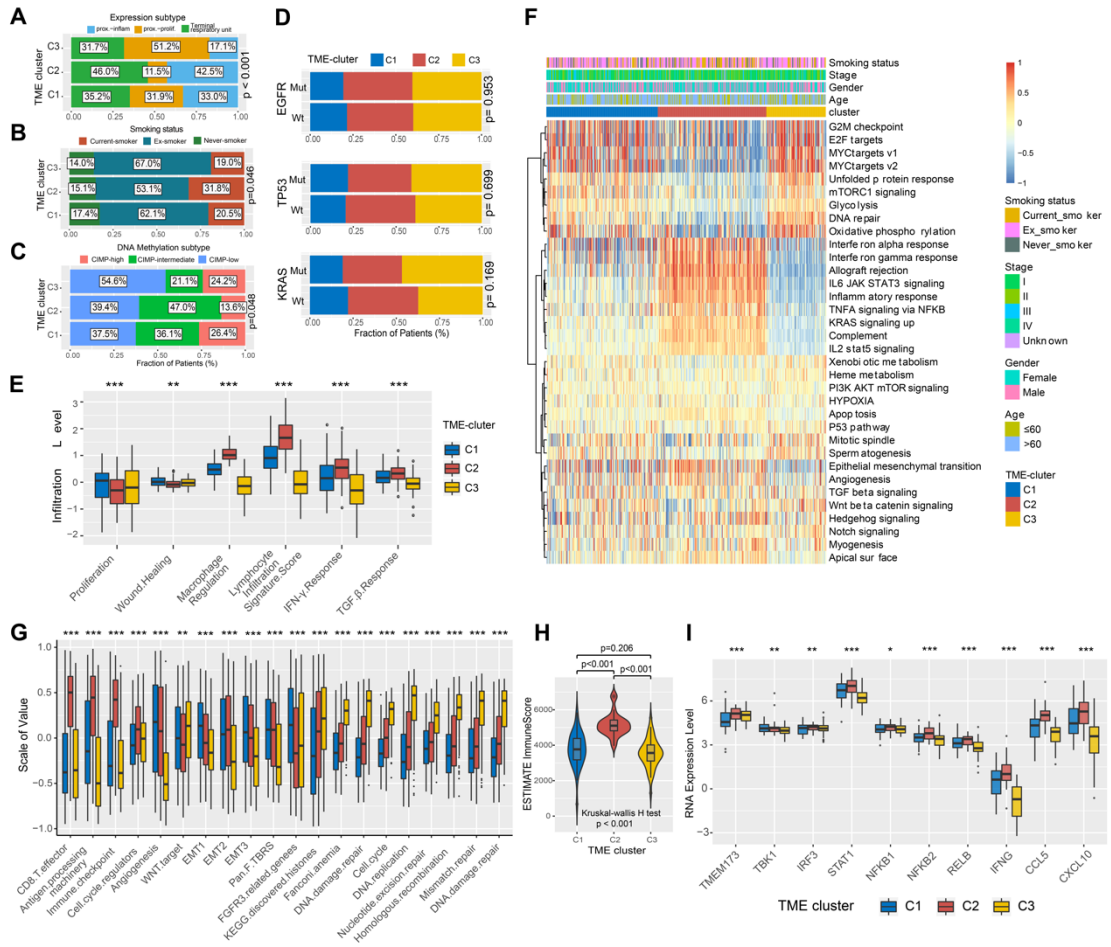

Supplemental Figure 3. The functional annotation of TME clusters. (A) The proportion of TCGA expression subtypes (PI, PP, and TRU) among three TME clusters. **(B)** The proportion of DNA methylation subtype (CIMP-high, intermediate, and low) among three TME clusters. **(C)** Cigarette smoking history among three TME clusters. **(D)** The mutational proportion of lung cancer driver genes of TP53, KRAS and EGFR among three TME infiltration patterns. **(E)** Differential distribution of three TME clusters in Thorsson et.al constructed six immune landscape signatures. **(F)** Heatmap shows the representative molecular pathways in distinct TME cell-infiltrating patterns in TCGA-LUAD cohort. **(G)** Differences of specific pathways curated from Mariathasan et al. constructed gene set among three distinct TME clusters. **(H)** Differences in Estimate-ImmuneScore among three TME clusters in CPTAC-LUAD

cohort. **(I)** Comparison of the mRNA expression of STING-related molecules in CPTAC-LUAD cohort. The Kruskal-Wallis test was used to compare the statistical difference between three TME clusters ($P < 0.001$). The thick line of the boxplot represented the median value.

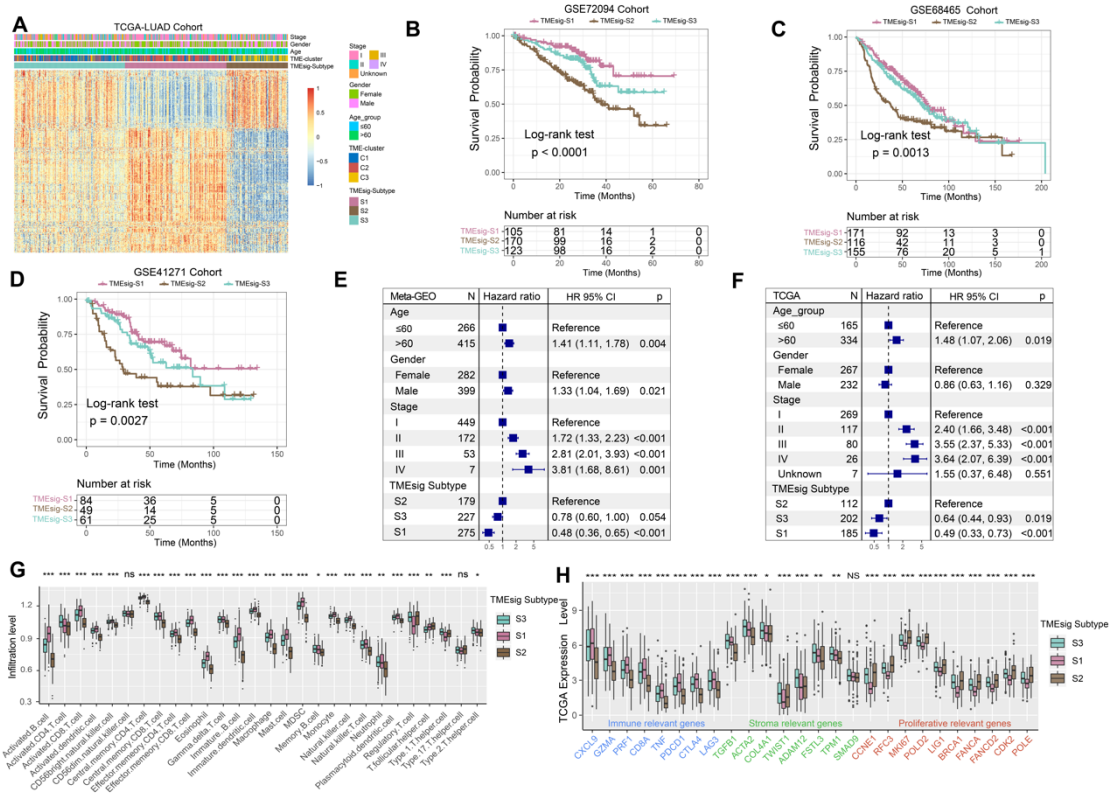

Supplemental Figure 4. Identification of TME phenotype-related gene signature subtypes in the NSCLC. (A) Unsupervised clustering of TME phenotype-related gene signatures to classify TCGA-LUAD patients into different transcriptomic subtypes, termed as TMEsig subtype S1-S3, respectively. The stage, gender, age, TME clusters and TME signature subtype were used as patient annotations. **(B-D)** Kaplan-Meier curves for survival of three TME signature subtypes in independent nonsquamous NSCLC cohorts (GSE72094, GSE68465, GSE41271). **(E-F)** Subgroup analysis estimating clinical prognostic value between TME gene signature subtype and clinical characteristics by multivariate Cox regression in meta-GEO **(E)** and TCGA cohort **(F)**. The length of the horizontal line represented the 95% confidence interval of hazard ratio (HR) for each variable. **(G)** Relative abundance of the Charoentong et.al curated immune cell subsets among TME gene signature subtypes. **(H)** The gene expression of

the immune-, stroma- and proliferative-relevant genes in three TME gene signature subtypes. The upper and lower ends of the boxes represented an interquartile range of values. The lines in the boxes represented the median value, and black dots showed outliers. The Kruskal-Wallis test was used to test the statistical differences among three gene signature clusters and the asterisks represented the statistical P-value (*P < 0.05; **P < 0.01; ***P < 0.001).

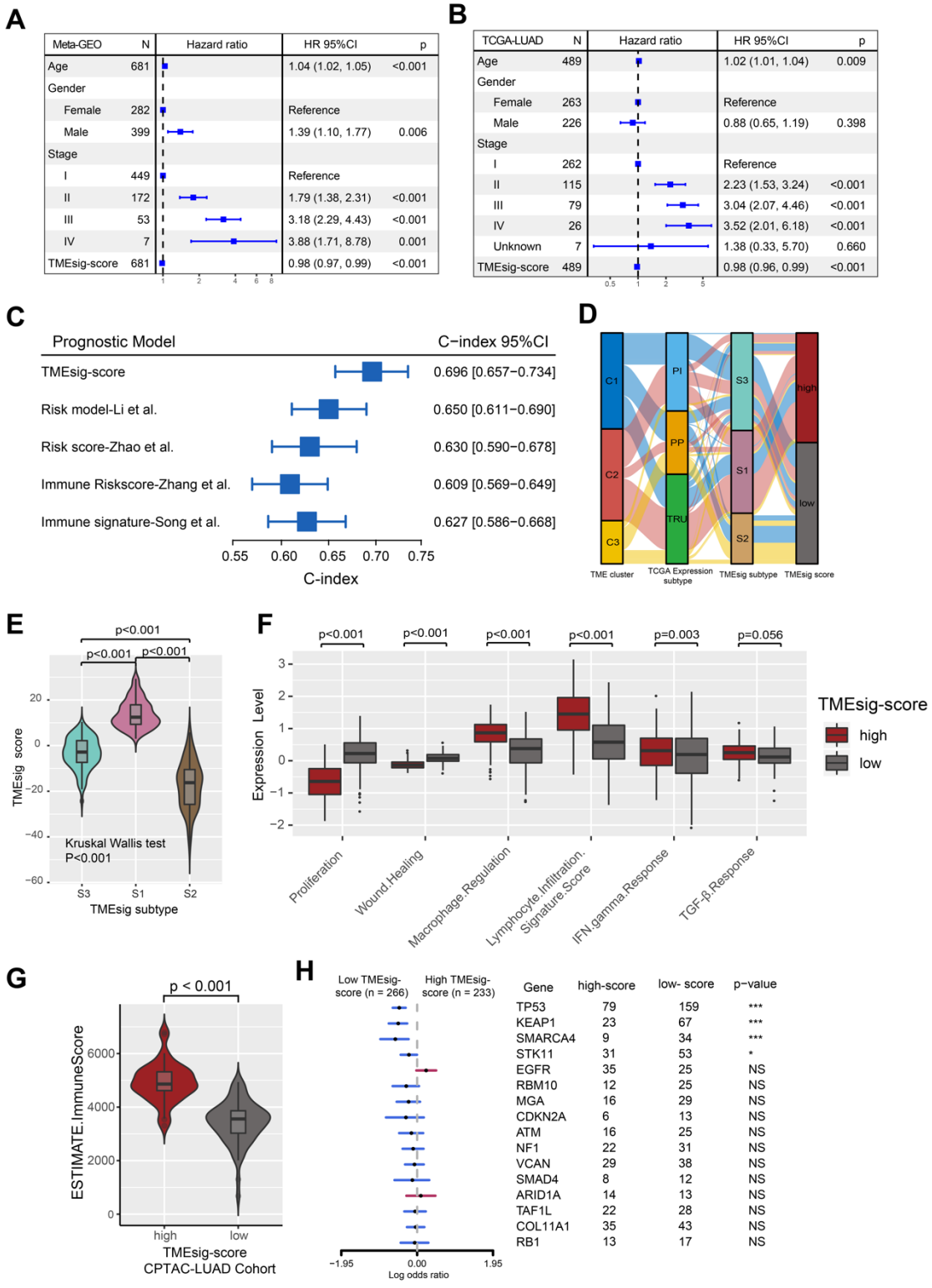

Supplemental Figure 5. TMEsig score associated with clinical characteristics and gene mutation. (A-B) Subgroup analysis estimating the clinical prognostic value of TME score in Meta-GEO **(A)** and TCGA-LUAD **(B)** cohort by multivariate Cox

regression. The length of the horizontal line which across the square represented the 95% confidence interval of hazard ratio (HR) for each variable. **(C)** Comparison of the concordance index (C-index) for survival time in five scoring system. **(D)** Differences in TMEsig score among three TMEsig subtype in TCGA-LUAD cohort ($P < 0.001$, Kruskal-Wallis test). **(E)** Alluvial diagram of NSCLC TMEsig-score in groups with TME clusters, expression subtypes (PI, PP and TRU) and TME-signature subtype. **(F)** Compared with patients with a low TMEsig score, the high TMEsig score subgroup had higher level of Lymphocyte infiltration signature score, Macrophage regulation, and IFN-γ response, but lower level of proliferation and wound healing. **(G)** Comparison of Estimate-ImmuneScore between high and low subgroup in CPTAC-LUAD cohort ($P < 0.001$, Wilcoxon rank sum test). **(H)** Compared with the high TMEsig score subgroup, the SMG mutational landscapes showed that *TP53*, *KEAP1, STK11* and *SMARCA4* had higher somatic mutation frequency in the low TMEsig score subgroup (Fisher's exact test).

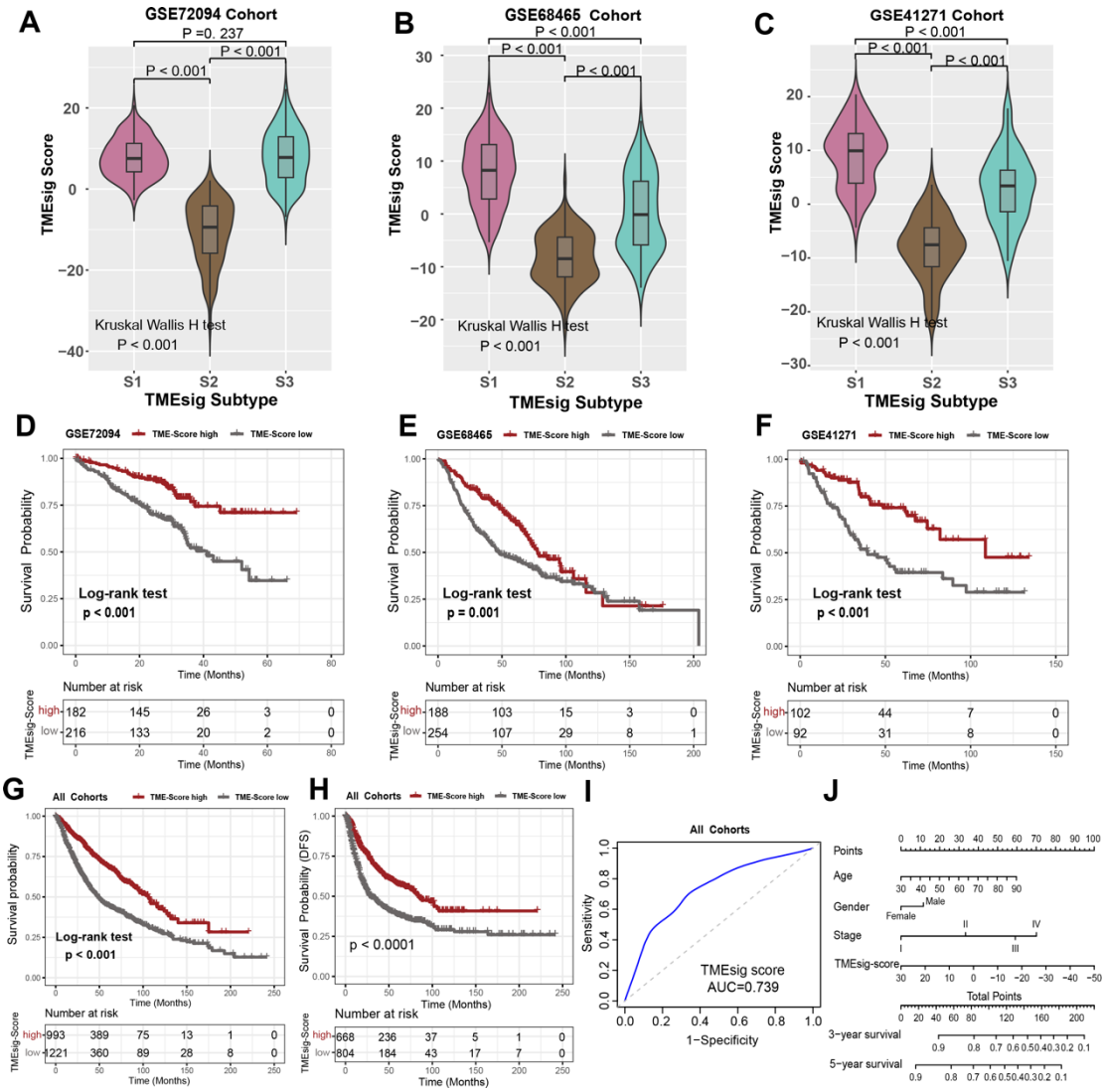

Supplemental Figure 6. High TMEsig score group exhibited significant clinical benefits. (A-C) Distributions of TMEsig-score in different TME signature subtypes in independent cohort, including GSE72094, GSE68465, and GSE41271. **(B-F)** Survival analysis of TMEsig score in nonsquamous NSCLC patients of independent cohorts. **(G-H)** The prognostic values of the TMEsig score on overall survival **(G)** and disease-free survival **(H)** were also validated in all collected nonsquamous NSCLC samples. **(I)** ROC curves analysis revealed the predictive advantage on prognosis of the established risk score model. **(J)** Nomogram to calculate the risk score of combined TMEsig score with clinical features and predict survival probability.

Full unedited gel for Figure 5J

cGAS, STING, p-STING, TBK1

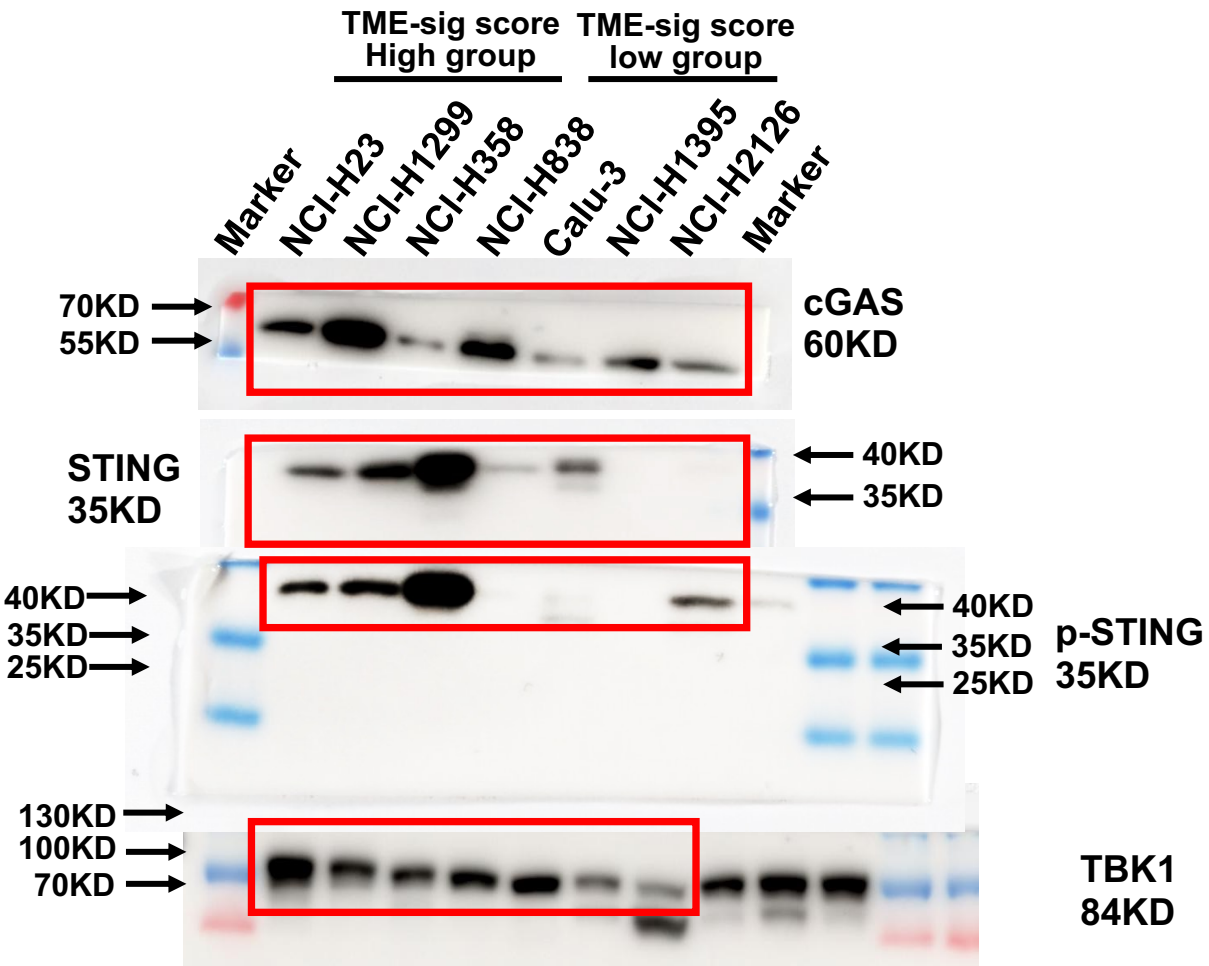

Full unedited gel for Figure 5J

NF-κB, p-NF-κB, IRF3, p-IRF3, CCL5, CXCL10, β-actin